Infinitely Adaptive Transition Metal Ordering in $Ln_2O_2MSe_2$-type Oxychalcogenides

Chris M. Ainsworth,(a) Chun-Hai Wang,(a) Hannah E. Johnston,(a) Emma E. McCabe,(a) Matthew G. Tucker,(b) Helen E. A. Brand,(c) John S. O. Evans*,(a,d)

(a)Department of Chemistry, University Science Site, Durham University, South Road, Durham, DH1 3LE, UK

(b)ISIS Neutron and Muon Source, Science and Technology Facilities Council, Rutherford Appleton Laboratory, Harwell Oxford, Didcot, OX11 0QX, UK

(c)Australian Synchrotron, 800 Blackburn Rd., Clayton, Victoria, 3168, Australia

(d)ANSTO (Australian Nuclear Science and Technology Organisation), New Illawarra Road, Rutherford Avenue, Lucas Heights, NSW 2234, Australia

ABSTRACT: A number of $Ln_2O_2MSe_2$ (Ln = La & Ce, M = Fe, Zn, Mn & Cd) compounds have recently been reported in the literature, built from alternating layers of fluorite-like $[Ln_2O_2]^{2+}$ sheets and antifluorite-like $[MSe_2]^{2-}$ sheets. The available $MSe_{4/2}$ tetrahedral sites are half occupied, and different compositions display different ordering patterns: $[MSe_2]^{2-}$ layers contain $MSe_{4/2}$ tetrahedra that are exclusively edge-sharing (stripe-like), exclusively corner-sharing (checkerboard-like), or mixtures of both. This paper reports 60 new compositions in this family. We reveal that the transition metal arrangement can be systematically controlled by either Ln or M doping leading to an "infinitely adaptive" structural family. We show how this is achieved in $La_2O_2Fe_{1-x}Zn_xSe_2$, $La_2O_2Zn_{1-x}Mn_xSe_2$, $La_2O_2Mn_{1-x}Cd_xSe_2$, $Ce_2O_2Fe_{1-x}Zn_xSe_2$, $Ce_2O_2Zn_{1-x}Mn_xSe_2$, $Ce_2O_2Mn_{1-x}Cd_xSe_2$, $La_{2-y}Ce_yO_2FeSe_2$, $La_{2-y}Ce_yO_2ZnSe_2$, $La_{2-y}Ce_yO_2MnSe_2$, and $La_{2-y}Ce_yO_2CdSe_2$ solid solutions.

KEYWORDS, mixed-anion, semiconductor, magnetism, powder diffraction, crystallography, solid solution.

INTRODUCTION

LaCuOS and analogous LnOCuCh (Ln = La–Nd, Bi; Ch = S, Se, Te) materials adopt the tetragonal ZrCuSiAs structure, space group *P4/nmm*. The structure is built up from alternating layers of fluorite-like $[Ln_2O_2]^{2+}$ sheets and antifluorite-like $[Cu_2Ch_2]^{2-}$ sheets.[1,2] There has been significant recent interest in materials with this structure type following the discovery of superconductivity at temperatures up to 55 K in LaOFeAs related systems.[3]

This paper discusses compounds related to LnOCuCh with divalent transition metal ions. This divalency leads to half occupancy of the transition metal sites, giving $[MSe_2]^{2-}$ layers, with different ordering patterns for different compounds. The first material reported with this composition, $Ce_2O_2MnSe_2$, was described as having 50% statistical occupancy of Mn on each site.[4] This arrangement retains the tetragonal space group *P4/nmm* of LnOCuCh-type compounds. Work in our group and by others[5,6] shows that this random distribution is incorrect and that the true structure is incommensurate with a complex pattern of occupancy of the tetrahedral $MSe_{4/2}$ sites. Nevertheless, the *P4/nmm* structure provides a useful parent or "subcell" model in which to initially identify ZrCuSiAs-related compounds, and from which to consider the structural relationships between the other known members of this family, Figure 1. $Ce_2O_2FeSe_2$ has $[FeSe_2]^{2-}$ layers containing 1-D chains of exclusively edge-sharing, (E, stripe-like) $FeSe_{4/2}$ tetrahedra,[7] while $La_2O_2CdSe_2$ has $[CdSe_2]^{2-}$ layers containing exclusively corner-sharing (C, checkerboard-like) $CdSe_{4/2}$ tetrahedra.[8] $La_2O_2ZnSe_2$,[9] $Ce_2O_2ZnSe_2$,[10] and $La_{0.44}Ce_{1.56}O_2MnSe_2$[5] have $[MSe_2]^{2-}$ layers containing sections of both stripe-like edge-sharing $MSe_{4/2}$ tetrahedra, and checkerboard-like corner-sharing $MSe_{4/2}$ tetrahedra, where the size of the checkerboard-like section increases from $La_2O_2ZnSe_2$ to $Ce_2O_2ZnSe_2$ to $La_{0.44}Ce_{1.56}O_2MnSe_2$. Using a simple nomenclature we can describe $La_2O_2ZnSe_2$ as 3C-1E, $Ce_2O_2ZnSe_2$ as 4C-1E and $La_{0.44}Ce_{1.56}O_2MnSe_2$ as 5C-1E. They can all be considered as intermediate structures between $Ce_2O_2FeSe_2$[7] and $La_2O_2CdSe_2$.[8] The disordered, stripe, checkerboard, 3C-1E and 4C-1E structures are illustrated in Figure 1. We and others have found that $Ce_2O_2MnSe_2$ has a closely related incommensurate structure, which we believe is best described in superspace group *Cmme*(α01/2)0s0, with modulation vector $\mathbf{q} = \alpha\mathbf{a}^* + 0\mathbf{b}^* + 0.5\mathbf{c}^*$ with $\alpha = 0.158(1)$.[5,6] In fact all of the structures reported to date can be derived from this modulated model as discussed below.

The structures reported to date for this family suggest that $Ln_2O_2MSe_2$ compounds may form an infinitely adaptive structural series,[11] where the details of the transition metal architecture in the $[MSe_2]^{2-}$ layers can be systematically tuned by chemical means. This can in turn potentially be used to tune electronic, optical and magnetic properties. In this paper we report 60 new compositions in the $La_{2-y}Ce_yO_2M_{1-x}M'_xSe_2$ (M = Fe, Zn, Mn & Cd) family which confirm this structural flexibility. We explore and discuss the origins of this effect and report detailed structural characterization for key samples to support our conclusions.

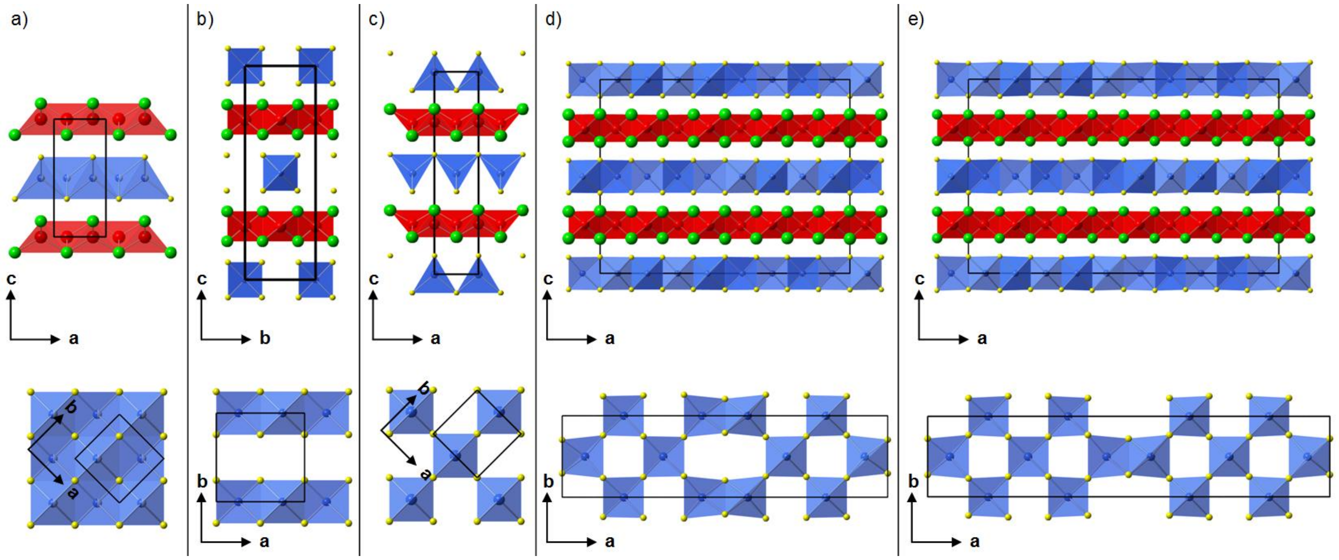

Figure 1. ZrCuSiAs-derived structures reported for (a) $Ln_2O_2MSe_2$, *P4/nmm* symmetry[4] (b) $Ce_2O_2FeSe_2$, *Imcb* symmetry[7] (c) $La_2O_2CdSe_2$, *P4₂/nmc* symmetry[8] (d) $La_2O_2ZnSe_2$, *Bmab* symmetry[9] (e) $Ce_2O_2ZnSe_2$, *Imcb* symmetry.[10] Top figures show the fluorite-like sheets of edge-sharing Ln_4O tetrahedra (red) and antifluorite-like sheets of MSe_4 tetrahedra (blue). Bottom figures are the view down [001], showing the arrangement of MSe_4 tetrahedra. Ln^{3+} cations are shown in green, O^{2-} anions in red, M^{2+} cations in blue and Se^{2-} anions in yellow.

EXPERIMENTAL SECTION

A range of $Ln_2O_2MSe_2$ materials were prepared as polycrystalline powders with Ln = La & Ce, M = Fe, Zn, Mn & Cd. All samples were prepared according to the equations below, using the appropriate reagents; La_2O_3 (99.99%, Sigma Aldrich, heated to 1000 °C before use) CeO_2 (99.99%, Alfa Aesar, heated to 1000 °C before use), Fe (99.9%, Sigma Adrich), Zn (99.9%, Alfa Aesar), Mn (99.9%, Koch-Light), Cd (99.5%, Alfa Aesar), Se (99.999%, Alfa Aesar), Al (99.5%, Alfa Aesar), Ti (99.5%, Alfa Aesar).

$$(1-\tfrac{y}{2})La_2O_3 + yCeO_2 + xM + (1-x)M' + 2Se + \left(\frac{2}{3}+\frac{1}{3}y\right)Al \rightarrow La_{2-y}Ce_yO_2M_xM_{(1-x)}'Se_2 + \left(\frac{1}{3}+\frac{1}{6}y\right)Al_2O_3$$

$$(1-\tfrac{y}{2})La_2O_3 + yCeO_2 + Mn + 2Se + \left(\frac{1}{2}+\frac{1}{4}y\right)Ti \rightarrow La_{2-y}Ce_yO_2MnSe_2 + \left(\frac{1}{2}+\frac{1}{4}y\right)TiO_2$$

Reagents were intimately ground and placed in an alumina crucible. Al or Ti powder (110% or 105% molar amount respectively) was placed in a second alumina crucible to act as an oxygen getter (OG), forming Al_2O_3/TiO_2 during the reaction. These two crucibles were placed in an evacuated ($<10^{-3}$ atm) silica tube and slowly heated to a final dwell temperature (1000, 1100 or 1200 °C) for a set time (12, 24 or 48 h) before cooling to room temperature. The composition, synthetic conditions and colors of all samples made are tabulated in Table S1 and Table S2.

X-ray powder diffraction (XRPD) data were collected using a Bruker D8 diffractometer operating in reflection mode with Cu $K\alpha_{1/2}$ radiation, a Lynxeye Si strip PSD, step size 0.02° and variable divergence slits. Samples were sprinkled onto Si zero-background slides covered with a thin layer of Vaseline. For initial phase identification and Pawley refinements (to derive cell parameters and modulation vectors), room-temperature data were collected for 30 min over a 2θ range 8–90°. Where more detailed structural information and/or XRPD patterns are presented, room temperature data were collected for 14 h over a 2θ range 8–120°.

For Rietveld analysis, NPD data were collected on the GEM diffractometer at ISIS for $Ce_2O_2Fe_{3/4}Zn_{1/4}Se_2$, $Ce_2O_2Fe_{1/8}Zn_{7/8}Se_2$, $Ce_2O_2Zn_{1/6}Mn_{5/6}Se_2$ and $La_2O_2Zn_{1/10}Mn_{9/10}Se_2$. The samples (~3.2, 2.4, 1.8 and 0.6 g respectively) were loaded into 6 mm diameter cylindrical vanadium cans and data acquired for 2 h at room temperature. Synchrotron data were collected on $Ce_2O_2CdSe_2$ loaded in a 0.3 mm capillary on the powder diffraction beamline at the Australian synchrotron.[12] Data were collected using the Mythen microstrip detector[13] from 1 – 81° 2θ with a wavelength of 0.6354462(7) Å. To cover the gaps between detector modules, 2 datasets were collected with the detector set 0.5° apart and then merged to a single dataset using in-house data processing software, PDViPeR,

For structure determination, powder diffraction data were analysed by the Rietveld method[14] using the Topas Academic (TA) software.[15-17] For $Ce_2O_2Fe_{3/4}Zn_{1/4}Se_2$, $Ce_2O_2Fe_{1/8}Zn_{7/8}Se_2$, $Ce_2O_2Zn_{1/6}Mn_{5/6}Se_2$ and $La_2O_2Zn_{1/10}Mn_{9/10}Se_2$, a combined X-ray and neutron (6 detector banks) refinement was carried out using room-temperature scans for the four samples discussed. The background (shifted Chebychev), sample height (DIFA/DIFC/ZERO for neutron refinements), peak profiles, a March Dollase unidirectional preferred orientation correction[18] along 001 (X-ray only), a Pitschke surface roughness correction,[19] lattice parameters, atomic positions, isotropic thermal parameters, neutron absorption correction, and a phase fraction of any minor Ln_2O_2Se impurity phase were refined. For $Ce_2O_2CdSe_2$, refinement of synchrotron X-ray data was carried out using room-temperature data on a phase-pure sample (synthesized at 1150 °C for 24 h with a Ti OG). The background (shifted Chebychev), sample height, peak profiles, coefficients of a Stephens' *hkl* dependent peak broadening correction,[20] lattice parameters, atomic positions, and isotropic thermal parameters were refined.

RESULTS

Synthesis and Phase Purity

A range of $Ln_2O_2M_{1-x}M'_xSe_2$ and $La_{2-y}Ce_yO_2MSe_2$ (Ln = La & Ce, M/M' = Fe, Zn, Mn & Cd) solid solutions were prepared to investigate the effects of systematically changing the relative sizes of $[Ln_2O_2]^{2+}$ and $[MSe_2]^{2-}$ layers on transition metal ordering. Samples were synthesized for 12, 24 or 48 h with an OG molar amount of 110 and 105% for Al and Ti respectively, at 1000, 1100 or 1200 °C. Specific synthetic conditions for each sample are tabulated in Table S1. XRPD showed that in most cases a layered ZrCuSiAs-related phase had formed with a unit cell $a = b \approx 4$ Å, $c \approx 9$ Å (the subcell), explaining the main peaks present. Weak additional reflections were observed at low angles for all samples which could not be attributed to known impurity phases. It is shown below that these arise from transition metal ordering.

The sample color varied significantly across the solid solutions. The colors of all samples are given in Table S2. In overview, the $La_2O_2Fe_{1-x}Zn_xSe_2$ samples are black/dark green, $La_2O_2Zn_{1-x}Mn_xSe_2$ pink/orange, $La_2O_2Mn_{1-x}Cd_xSe_2$ brick red/brown, $Ce_2O_2Fe_{1-x}Zn_xSe_2$ black, $Ce_2O_2Zn_{1-x}Mn_xSe_2$ dark red, $Ce_2O_2Mn_{1-x}Cd_xSe_2$ dark red/red, $La_{2-y}Ce_yO_2FeSe_2$ black, $La_{2-y}Ce_yO_2ZnSe_2$ black/ochre $La_{2-y}Ce_yO_2MnSe_2$ dark red/black, and $La_{2-y}Ce_yO_2CdSe_2$ ochre.

There are a few cases across the different solid solutions where the orthorhombic β-$Ln_2O_2MSe_2$ polymorph[21] (referred to as the *oP*-$Ln_2O_2MSe_2$ polymorph by others[6,22]) formed in preference to the layered ZrCuSiAs-related structure. We refer to this structure type as the "β phase" throughout, and the regions where it forms are indicated in Figure 2.

The layered/β phases account for >95% weight percentage in most of the samples prepared. Minor additional impurities typically include Ln_2O_2Se and MSe phases. Table S1 gives the weight percentages of the phases formed for all samples discussed.

Unit Cell Volume Trends

The cell volume of layered ZrCuSiAs-related phases in all six $Ln_2O_2M_{1-x}M'_xSe_2$ solid solutions prepared are shown in Figure 2 (left). Series with common end members have been plotted continuously, and the plot is ordered Fe–Zn, Zn–Mn, Mn–Cd to reflect increasing effective transition metal radius for this structure type. For the small number of compositions reported previously we have included data points from the literature.[5-10,22] This gives one continuous plot for the three Ce solid solutions $Ce_2O_2Fe_{1-x}Zn_xSe_2$, $Ce_2O_2Zn_{1-x}Mn_xSe_2$ and $Ce_2O_2Mn_{1-x}Cd_xSe_2$, and for the three La solid solutions $La_2O_2Fe_{1-x}Zn_xSe_2$, $La_2O_2Zn_{1-x}Mn_xSe_2$ and $La_2O_2Mn_{1-x}Cd_xSe_2$.

Shannon's tables give ionic radii values of Fe = 0.63, Zn = 0.6, Mn = 0.66 and Cd = 0.78 Å, for 4 coordinate +2 oxidation states.[23] These values broadly account for the cell volume trends observed, though there are more subtle anomalies. Firstly, the cell-volume gradient in Fe/Zn solid solutions is slightly positive; ionic radii consideration alone would suggest this should be negative. This could be caused by small amounts of Fe^{3+} being present, or by the changes in transition metal ordering discussed below. Secondly, the positive volume gradient of Zn–Mn and Mn–Cd containing solid solutions is roughly equal. This is somewhat surprising given the smaller difference in ionic radii between Zn and Mn compared to Mn and Cd (0.06 vs 0.12 Å).

For the Ce systems we have recently shown that the cell volume is influenced by the Ce^{3+}:Ce^{4+} ratio in the material (we presume the charge compensation mechanism is minor transition metal loss).[10] This can be controlled by the amount of OG used, which affects the amount of O available to the system. This effect was also observed in $La_{0.2}Ce_{1.8}O_2ZnSe_2$ (for example, the gray data points in Figure 2 are for samples synthesized with 100% and 95% Al molar amount), and will presumably occur in many/all of these systems. It is also the most likely reason for the higher scatter of Ce cell volumes across solid solutions (relative to La compounds) in Figure 2. Attempts to deliberately change the cell volume of La-containing compounds were unsuccessful, consistent with the fixed +3 oxidation state of La.

The cell volumes of layered phases in the four $Ln_{2-y}Ce_yO_2MSe_2$ solid solutions studied are shown in Figure 2 (right). The gradient of all curves is negative, as expected from the lanthanide contraction. This effect will be enhanced by small levels of Ce oxidation. As in the $Ln_2O_2M_{1-x}M'_xSe_2$ solid solutions, Fe-containing compounds have a smaller cell volume than analogous Zn compounds.

Under the experimental conditions used, partial β phase formation occurs for $La_2O_2Fe_{1-x}Zn_xSe_2$ with $x < 0.33$, with near pure β phase formation for $x < 0.25$. $La_2O_2MnSe_2$ also preferentially forms the β phase, though only slight Zn or Cd doping is required ($x \approx 0.05$ and 0.1 respectively) for the layered structure to form. The β phase also begins to form in place of the layered structure in $La_{2-y}Ce_yO_2FeSe_2$ (for $y \lesssim 0.5$) and $La_{2-y}Ce_yO_2MnSe_2$ (onset $y \approx 0.7$). Recent work on $Ln_2O_2FeSe_2$ and $Ln_2O_2MnSe_2$ (Ln = La, Ce) shows that single crystals of the La and Ce structures can be prepared in the 2D phase by careful control of the synthesis conditions.[6,22] Data from these works are shown with open points in Figure 2.

Cell Parameter Trends

The individual cell parameters of 2D phases in the six $Ln_2O_2M_{1-x}M'_xSe_2$ solid solutions are shown in Figure 3. These were derived using a $\sqrt{2}a_{\text{subcell}} \times \sqrt{2}b_{\text{subcell}} \times 2c_{\text{subcell}}$ unit cell. For comparison each has been normalised to the cell parameter of the zinc phase $Ln_2O_2ZnSe_2$.[9] By comparing this figure with Figure 2, it is apparent that the majority of the volume change on M substitution is due to changes in the *c*-axis, perpendicular to the layers.

The cell parameters in the four $Ln_{2-y}Ce_yO_2MSe_2$ solid solutions are shown in Figure 4. In contrast to transition metal substitution, lanthanide substitution leads to significant changes in all cell parameters, with *a* and *b* changing at approximately twice the rate of the *c*-axis.

The trends in both the $Ln_2O_2M_{1-x}M'_xSe_2$ and $La_{2-y}Ce_yO_2MSe_2$ solid solutions show that the Ln-O layers are relatively rigid, and the M-Se layers relatively flexible. The M-Se layers can therefore adapt to the size demands of the Ln-O layer. This is discussed in more detail below.

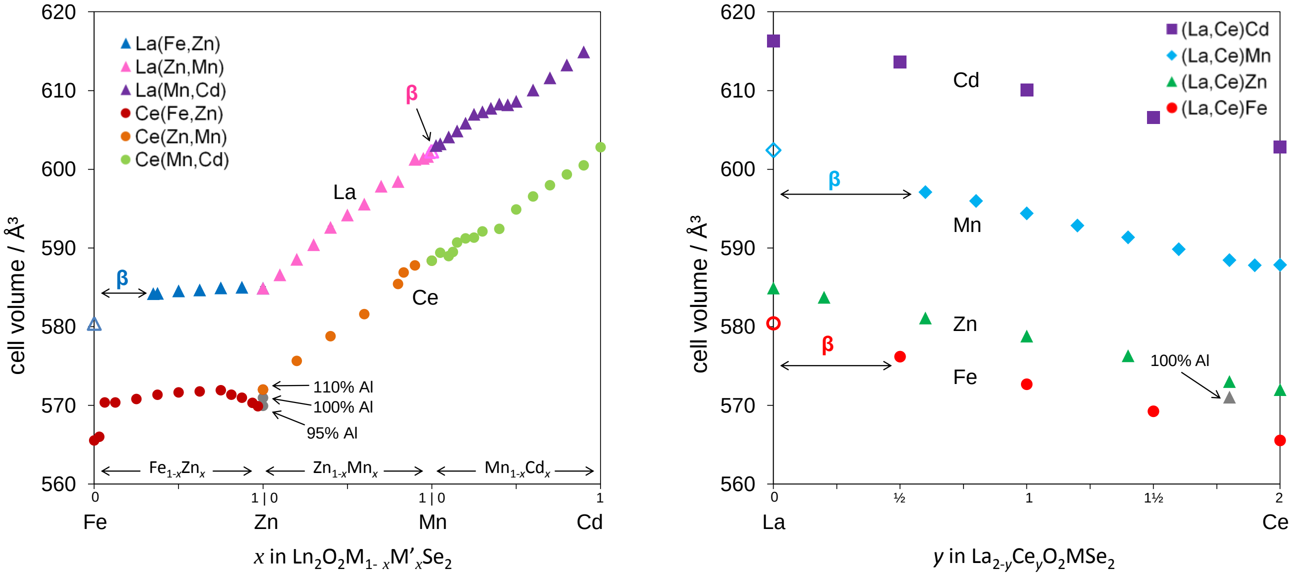

Figure 2. Cell volume of 2D ZrCuSiAs-related phases in $Ln_2O_2M_{1-x}M'_xSe_2$ (left) and $Ln_{2-y}Ce_yO_2MSe_2$ (right) solid solutions. The $La_2O_2FeSe_2$/ $La_2O_2MnSe_2$ data points (open symbols) are taken from the literature.[6,22] Rietveld error bars are smaller than data points.

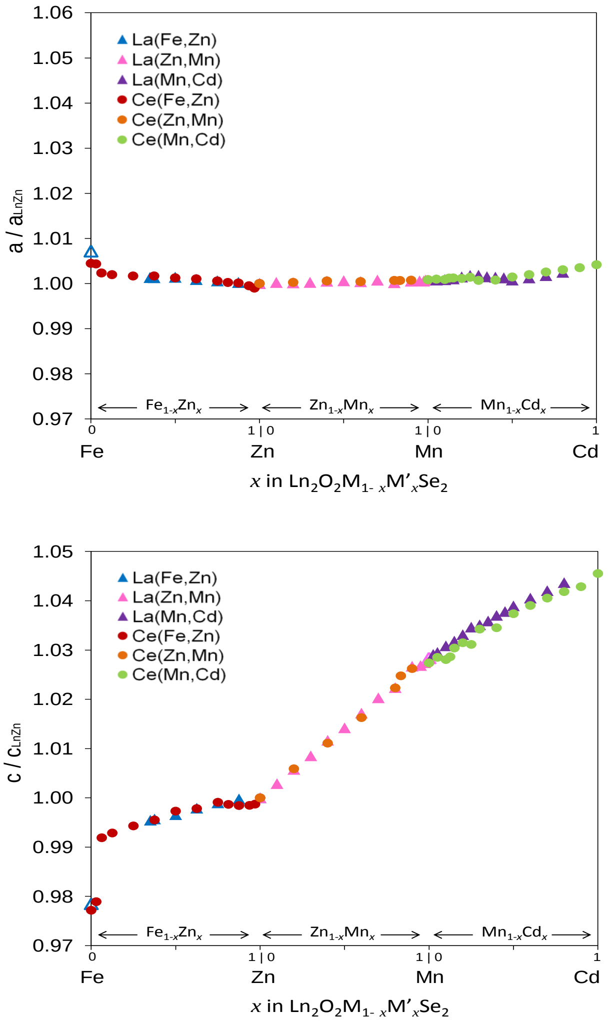

Figure 3. Relative cell parameters of 2D $Ln_2O_2M_{1-x}M'_xSe_2$ solid solutions. Changes in *b* parameter follow *a* parameter. Rietveld error bars are smaller than data points.

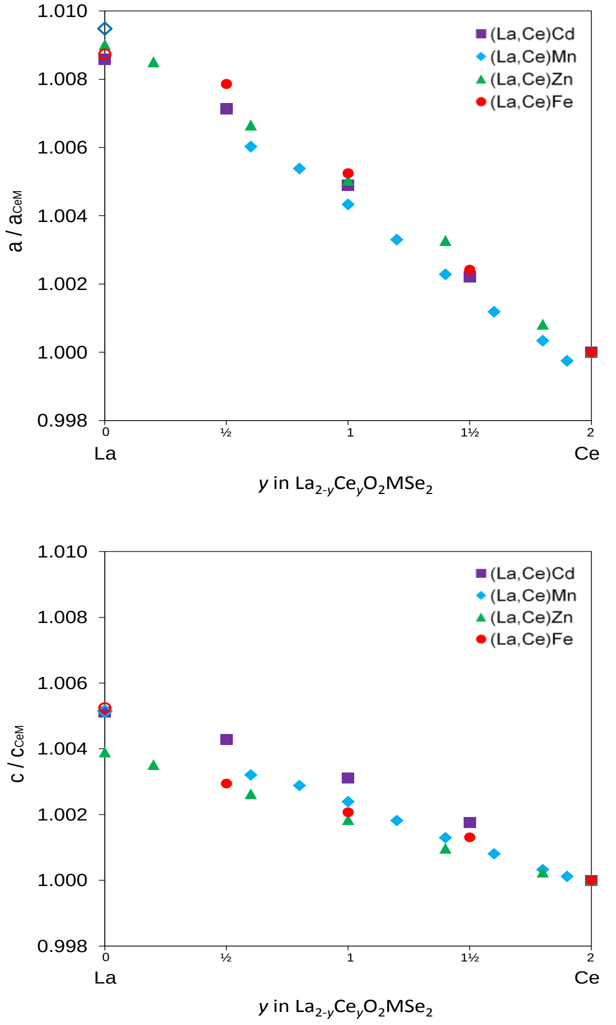

Figure 4. Relative cell parameters of 2D $Ln_{2-y}Ce_yO_2MSe_2$ solid solutions. Changes in *b* parameter follow *a* parameter. Rietveld error bars are smaller than data points.

Modulation Vector Investigation

All known commensurately ordered $Ln_2O_2MSe_2$-type compounds to date can be described with a unit cell with dimensions $n\sqrt{2}a_{\text{subcell}} \times \sqrt{2}b_{\text{subcell}} \times 2c_{\text{subcell}}$, where n = 1 ($Ce_2O_2FeSe_2$,[7] 0C-1E), n = 4 ($La_2O_2ZnSe_2$,[9] 3C-1E), n = 5 ($Ce_2O_2ZnSe_2$,[10] 4C-1E) or n = 6 ($La_{0.44}Ce_{1.56}O_2MnSe_2$,[5] 5C-1E). These systems can therefore be described as an evolving series using a modulated approach based on a $\sqrt{2}a_{\text{subcell}} \times \sqrt{2}b_{\text{subcell}} \times 2c_{\text{subcell}}$ parent cell with a modulation vector of $\mathbf{q} = \alpha\mathbf{a}^* + 0\mathbf{b}^* + \frac{1}{2}\mathbf{c}^*$ and superspace group $Cmme(\alpha 01/2)0s0$. The corresponding $\mathbf{q}$-vectors for the commensurate structures are α = 1 (0C-1E), α = 1/4 (3C-1E), α = 1/5 (4C-1E), α = 1/6 (5C-1E), as shown schematically in Figure 5. Note that for an mC-1E structure $\alpha = 1/(m+1)$. We see no experimental evidence to adopt the lower symmetry $P112/n(\alpha\beta\frac{1}{2})0s$ suggested by others.[6]

For each of the samples reported in Figure 2 we have used the modulation approach to fit the weak unindexed satellite peaks observed in their powder pattern. This was performed by using the Pawley method to fit the subcell peaks and determine the subcell parameter. Up to 34 of the strongest satellite reflections were simultaneously fitted using a pseudo-Voigt peakshape at positions constrained by refining the magnitude of α. A typical fit is included in Figure S1.

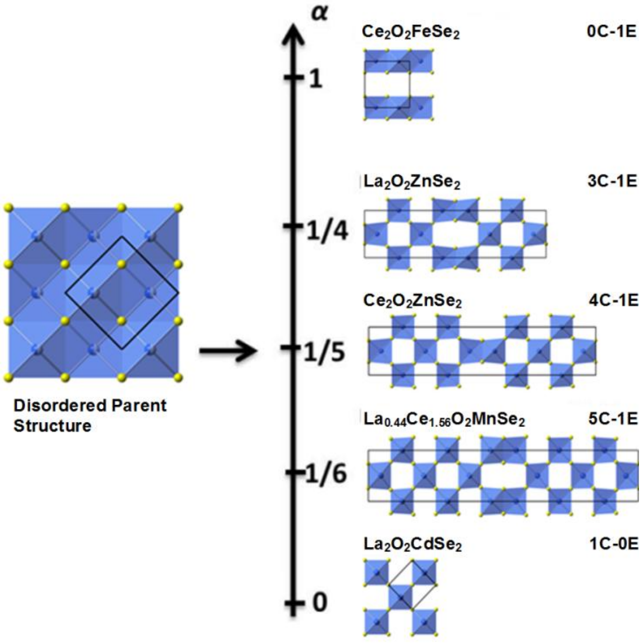

Figure 5. Relationship of transition metal ordering patterns in $Ln_2O_2MSe_2$.

Figure 6 shows the value of α (in $\mathbf{q} = \alpha\mathbf{a}^* + 0\mathbf{b}^* + 0.5\mathbf{c}^*$) over the six $Ln_2O_2M_{1-x}M'_xSe_2$ solid solutions, presented in the same sequence as Figure 2. As the effective transition metal radius is increased going from left to right, there is a systematic decrease in α in both La and Ce series. A decrease in α corresponds to an increase in the ratio of corner:edge sharing tetrahedra in mC-1E.

For the smallest M = Fe case both the La and Ce 2D materials adopt the 0C-1E structure with α = 1. Upon doping with a small amount of Zn ($x \leq 0.06$), α = 1 (0C-1E) transforms to α = 1/4 (3C-1E). The modulation vector appears to then lock in to this commensurate value, with α = 1/4 over a range of x in both the La and Ce series. For the Ce series, as the average radius of M is increased further ($x > 0.5$ in $Fe_{1-x}Zn_x$) α changes smoothly from 1/4 to 1/5 (x~0.8) then locks in to this value up to $Zn_{0.6}Mn_{0.4}$. α then changes smoothly before a small lock-in region at α = 1/6. There appears to be no locking in to commensurate ordering beyond this point. Instead there is a rapid progression through compounds with a continuously increasing ratio of corner- to edge-sharing $MSe_{4/2}$ tetrahedra. Very similar behavior is seen for the La series but with a small "lag" relative to Ce due to the larger radius of La than Ce. The stability field of the α = 1/4 structure is larger than for Ce, but there is no evidence for a lock-in phase at α = 1/6.

The evolution of α for $La_{2-y}Ce_yO_2MSe_2$ compounds is shown in Figure 7. All pure Fe containing compounds show one extreme of ordering with α = 1 (0C-1E), for all x. We know, however, from the $Ce_2O_2Fe_{1-x}Zn_xSe_2$ solid solution of Figure 6 that 0C-1E ordering is lost upon ~5% Zn doping, suggesting that pure $FeSe_{4/2}$ layers are important for realizing exclusively edge-sharing tetrahedra. This suggests that Fe–Fe bonding could help stabilize this structure type. For Zn-containing compounds, α = 1/4 for $0 < y \leq 1.4$. For $1.4 \leq y < 2$, α decreases gradually, then appears to be commensurate again at y = 2, with α = 1/5. For the larger Mn compounds, the tendency to "lock in" to commensurate ordering is lower. Instead, a series of incommensurate compounds form, passing through an effectively commensurate example with α = 1/6 at x = 1.56; $La_{0.44}Ce_{1.56}O_2MnSe_2$ can thus be described with 5C-1E ordering. Exclusively Cd-containing compounds exhibit the second extreme of transition metal ordering, and contain corner-sharing tetrahedra, 1C-0E.

Refinement of Commensurate Structures

To confirm the transition metal ordering patterns proposed as structures evolve across these series we have selected four samples from the $Ln_2O_2M_{1-x}M'_xSe_2$ solid solutions for detailed X-ray and neutron structural studies. Each has an α value corresponding to a lock-in or commensurate structure. These included the Ce containing compounds $Ce_2O_2Fe_{3/4}Zn_{1/4}Se_2$ (α = 1/4), $Ce_2O_2Fe_{1/8}Zn_{7/8}Se_2$ (α = 1/5), and $Ce_2O_2Zn_{1/6}Mn_{5/6}Se_2$ (α = 1/6) which represent 3C-1E, 4C-1E and 5C-1E structure types respectively, and the La containing compound $La_2O_2Zn_{1/10}Mn_{9/10}Se_2$ (α = 1/5), a second example of 4C-1E. Non-standard space groups were used in all cases to keep the c-axis perpendicular to the layers for consistency with other structures of this type reported in the literature. These were $Bmeb$ for the 3C-1E and 5C-1E structures, and $Imcb$ for the 4C-1E structure. As discussed elsewhere,[5,10] the structures could be described in lower symmetry settings, (with the loss of the mirror plane perpendicular to the a-axis), but this is beyond the information content of the powder diffraction data. We refined a total of 27, 32, 37 and 32 structural variables for $Ce_2O_2Fe_{3/4}Zn_{1/4}Se_2$, $Ce_2O_2Fe_{1/8}Zn_{7/8}Se_2$, $Ce_2O_2Zn_{1/6}Mn_{5/6}Se_2$, and $La_2O_2Zn_{1/10}Mn_{9/10}Se_2$ along with parameters to describe peak shapes and background functions for the X-ray and 6 banks of neutron diffraction data. In all cases, transition metal sites were found to be fully occupied or fully empty within the quality of the data, and a single isotropic temperature factor was used for each atom type. In all cases an excellent fit to the powder data was obtained and the intensity and positions of key superstructure reflections were well described confirming our structural models. Rietveld plots of X-ray data highlighting regions with superstructure reflections are shown in Figure 8. All refinement profiles and full structural parameters can be found in Table S4-S7 and Figure S2-S5.

Synchrotron powder data were also collected for $Ce_2O_2CdSe_2$, a previously unreported quaternary oxychalcogenide. It is isostructural to $La_2O_2CdSe_2$,[8] space group $P4_2/nmc$, with $[CdSe_2]^{2-}$ layers containing exclusively corner-sharing $CdSe_{4/2}$ tetrahedra (α = 0, 1C-0E). We refined a total of 10 structural variables along with parameters to describe peak shapes and background functions. Transition metal sites were found to be fully occupied or fully empty within the quality of the data, and isotropic temperature factors were used for each atom type. The refinement profile and full structural parameters can be found in Table S8 and Figure S6.

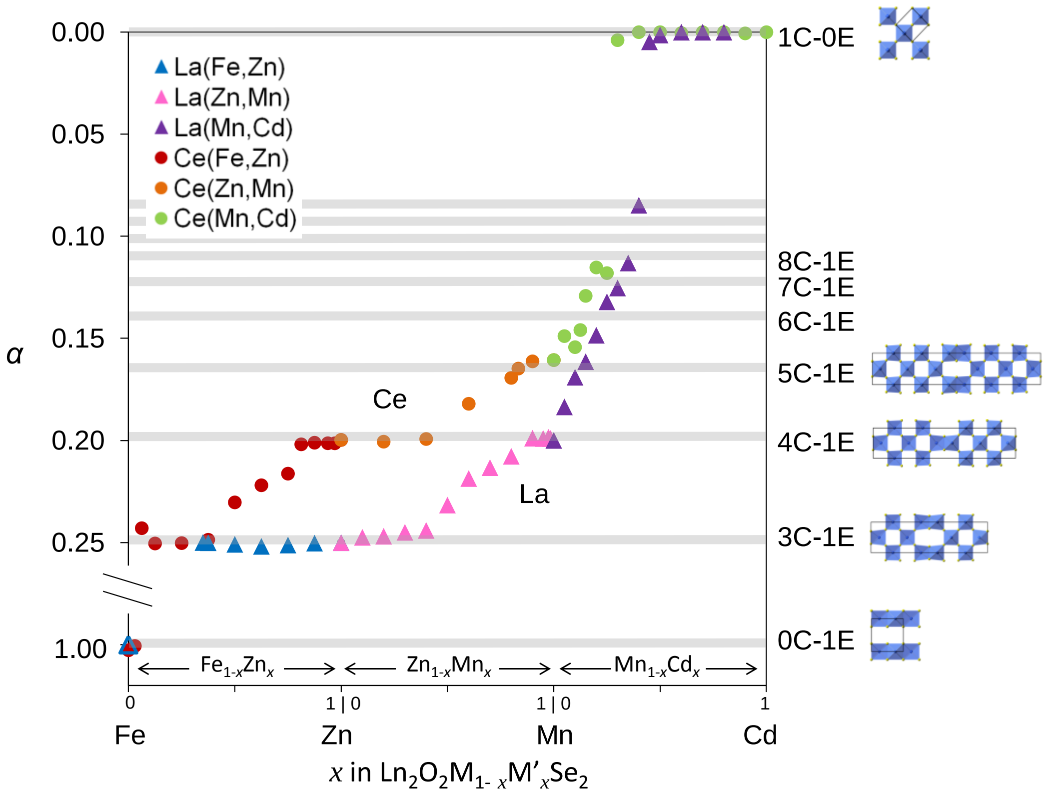

Figure 6. Modulation vector α for layered $Ln_2O_2M_{1-x}M'_xSe_2$ solid solutions. Grey bands represent commensurate ordering. The $La_2O_2FeSe_2$/$La_2O_2MnSe_2$ data points (open symbols) are taken from the literature.[6,22] Rietveld-derived error bars are smaller than individual data points.

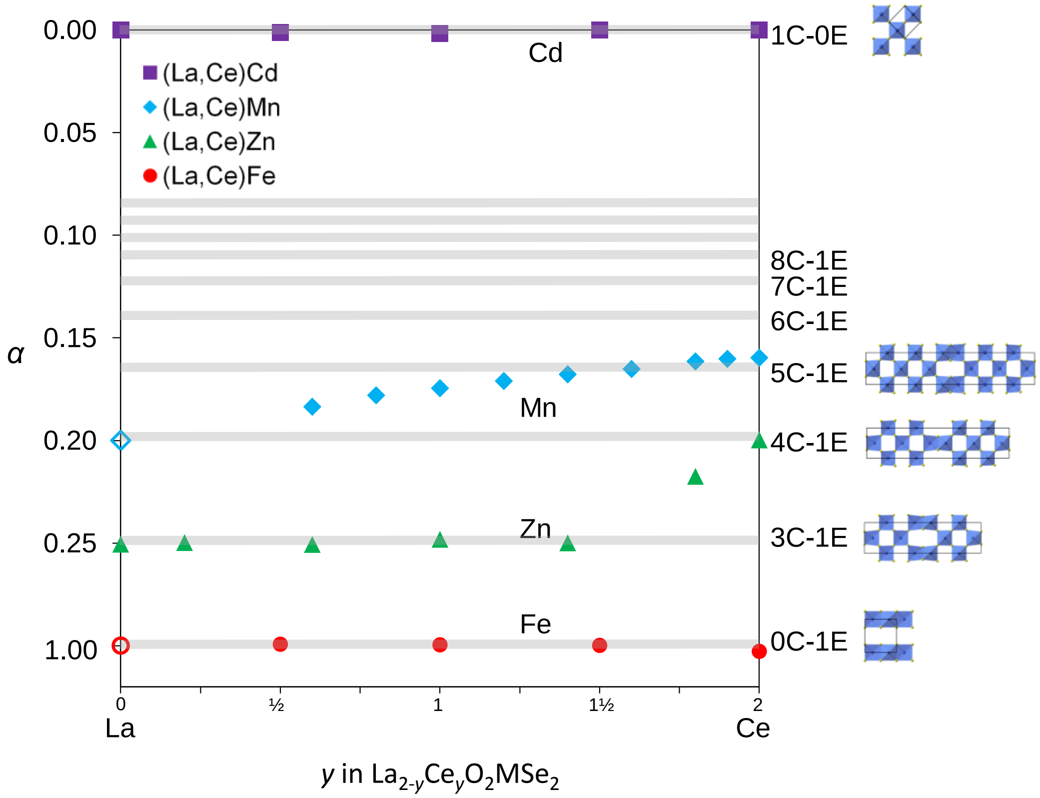

Figure 7. Modulation vector α for layered $Ln_{2-y}Ce_yO_2MSe_2$ solid solutions. Grey bands represent commensurate ordering. The $La_2O_2FeSe_2$/$La_2O_2MnSe_2$ data points (open symbols) are taken from the literature.[6,22] Rietveld-derived error bars are smaller than data points.

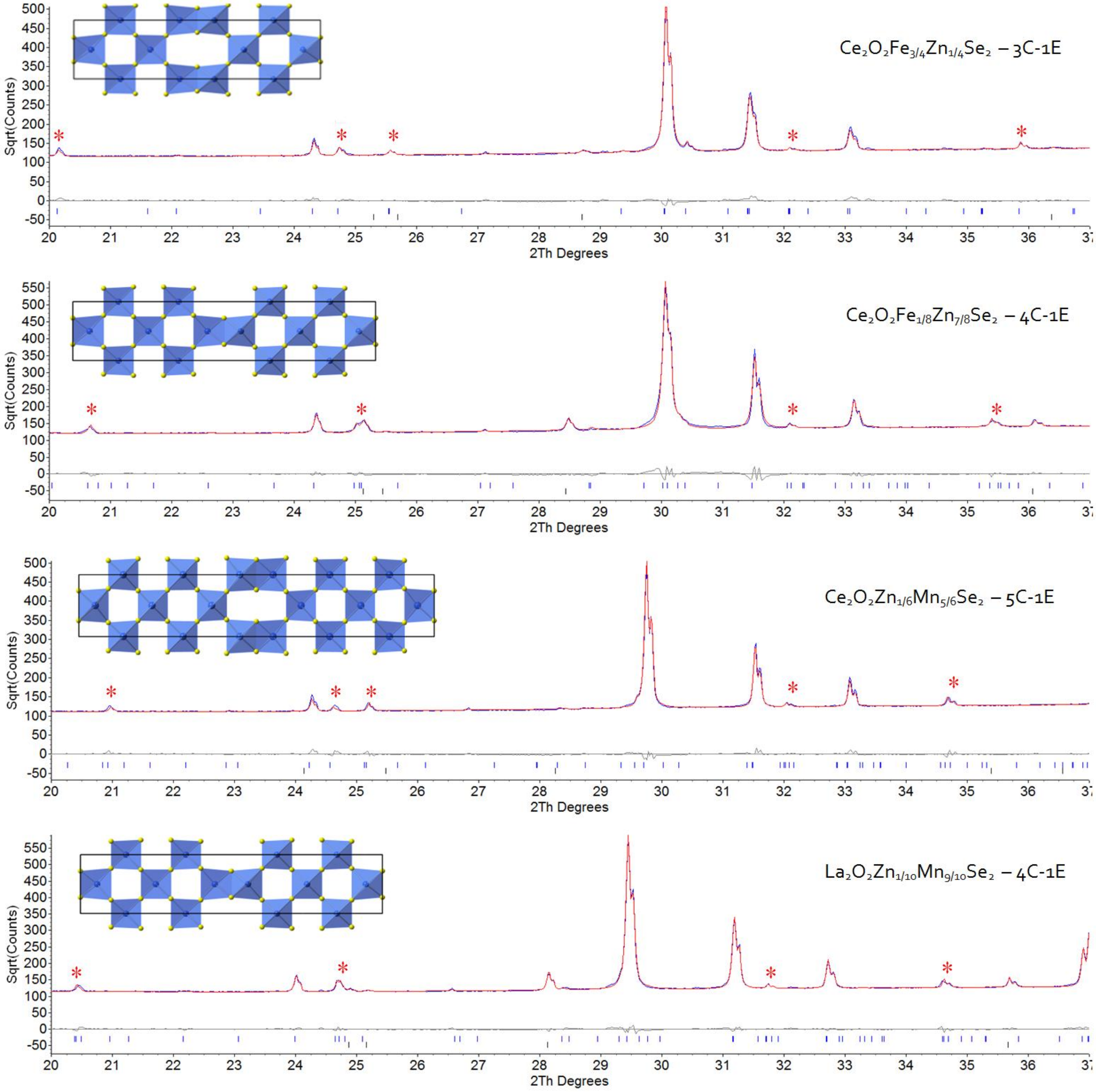

Figure 8. X-ray Rietveld profiles from combined X-ray and neutron refinements of selected commensurate samples from the $Ln_2O_2M_{1-x}M'_xSe_2$ series. Data are plotted on a $\sqrt{I}$ scale to emphasize weak supercell reflections, which are marked with an asterisk.

DISCUSSION

The information on the changes in unit cell parameters, modulation vector and detailed structure described above give significant insight into the structural chemistry of $Ln_2O_2MSe_2$ materials.

Firstly, it is clear from Figure 3 that a given edge-sharing $[Ln_2O_2]^{2+}$ tetrahedral layer is relatively rigid, with its size and geometry insensitive to the transition metal layer to a first approximation. It is, however, important to note that the $OLn_{4/2}$ edge-shared tetrahedra are not ideal but significantly compressed along the *c*-axis. This is common to $Ln_2O_2MSe_2$ and related LnOMCh materials as shown by the tetrahedral bond angles summarized for our end-member compounds in Table S9.[1,3,7-10,22,24] The $[Ln_2O_2]^{2+}$ rigidity means that as the radius of M is increased, the *a*/*b* cell parameters remain essentially unchanged, and the unit cell volume increase is largely due to a change in the *c*-axis as the $[Ln_2O_2]^{2+}$ layers move further apart.

The fact that structural distortions occur primarily in the $[MSe_2]^{2-}$ layers can also be seen from Figure 9, which shows the thickness along the *c*-axis of Ln-O-Ln, Se-Ln-O-Ln-Se and Se-M-Se blocks for structurally characterized samples[5-10,22] with increasing sizes of M. The thickness of the $[Ln_2O_2]^{2+}$ and $[Ln_2O_2Se_2]^{2-}$ block shows little change across the series whereas there is a systematic and significant increase in the thickness of the $[MSe_2]^{2-}$ block.

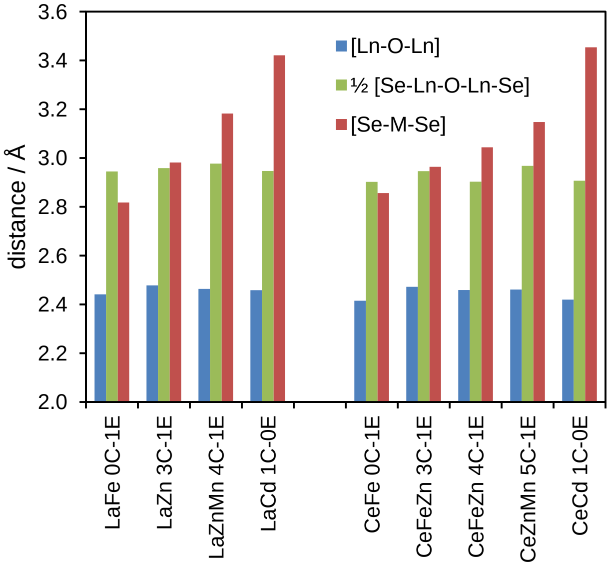

Figure 9. The thickness along the *c*-axis of Ln-O-Ln, Se-Ln-O-Ln-Se and Se-M-Se blocks for structurally characterized samples[5-10,22] with increasing sizes of M.

This flexibility reflects the fact that MSe_2 layers can respond to the fixed $[Ln_2O_2]^{2+}$ size in different ways. If we focus on the $La(Zn_{1-x}Mn_x)$ series, we observe a lock-in region for $0 < x < 0.5$ where the $\alpha = 1/4$ (3C-1E) structure is retained and the cell volume undergoes a gradual Vegard-like increase. The increase in the *c*-axis implies a gradual distortion of $MSe_{4/2}$ in this region. For $x > 0.5$, however, the change in modulation vector α ($\mathbf{q} = \alpha\mathbf{a}^* + 0\mathbf{b}^* + 0.5\mathbf{c}^*$) shows that the structure responds in a different way and that the ratio of corner- to edge-shared tetrahedra is systematically increased from 3C-1E to 4C1E (and to 5C-1E and beyond as Cd is introduced). A similar effect is seen for the Ce series but the lock in region is $\alpha = 1/5$ (4C-1E) for $0 < x < 0.5$, rising to $\alpha = 0.158$ (5.33C-1E) for $x = 1$.

The change in transition metal architecture can be explained by the fact that corner-shared tetrahedra are a more compact way of occupying 2-dimensional space than edge-shared tetrahedra. Therefore, as the size of the $[MSe_2]^{2-}$ block is increased relative to the $[Ln_2O_2]^{2+}$ block (either by increasing M or decreasing Ln radius) the proportion of corner-sharing tetrahedra will increase.

The local structural changes allowing the flexibility can be understood by considering the structure in terms of rows of Se atoms perpendicular to the *a*-axis of the modulated structures (e.g. 3C-1E and 4C-1E structures in Figure 1). We see that these rows repeat every $a_{\text{subcell}}/\sqrt{2}$ ~ 2.82 Å. Typical values of edge- and corner-shared M–M distances are, for example, 3.1 Å and 4.0 Å in $Ce_2O_2ZnSe_2$[10] and 3.2 and 4.0 Å in $Ce_2O_2MnSe_2$.[5] A corner sharing $MSe_{4/2}$ arrangement leads to rows of transition metals along *a* separated by M-M/$\sqrt{2}$ ~ 2.82 Å, whereas edge-sharing leads to rows separated by ~3.1 Å. Introduction of edge-sharing tetrahedra, which distort due to M–M proximity, therefore allows the $[MSe_2]^{2-}$ layer to expand to size-match the $[Ln_2O_2]^{2+}$ layers.

Figure 2 and Figure 3 show that the volume change across the $Zn_{1-x}Mn_x$ and $Mn_{1-x}Cd_x$ solid solutions is approximately equal (or perhaps slightly higher for the former than the latter), despite the larger difference in ionic radius for the Mn/Cd pair; this goes against Vegard's law expectations. The modulation vector plot of Figure 6 shows, however, that this can be explained by the constantly evolving value of α, and therefore constantly increasing proportion of smaller corner-sharing units in the (Mn/Cd) case.

As discussed above, the 0C-1E structure is favored for pure-Fe containing samples. This suggests that Fe–Fe bonding could help stabilize this structure type, and is consistent with the known tendency of FeSe to adopt structures such as the superconducting PbO-type polymorph with layers of edge-sharing tetrahedra, and a NiAs-type polymorph with face-shared octahedra; both structures encourage Fe–Fe bonding.[25] The observation that the cell parameter parallel to the chain direction is smaller than that perpendicular ($a < b$) gives some support to this observation. It is also clear from Figure 2 that the cell volumes of 0C-1E structures are significantly lower than those with corner-sharing. Whilst it's tempting to ascribe this to Fe–Fe bonding, the main contribution to the volume reduction is a ~1% contraction of the c-axis relative to other structures, suggesting the origins are more complex.

The $Ln_2O_2MSe_2$ materials therefore emerge as an infinitely adaptive set of structures with the $[MSe_2]^{2-}$ layers responding to changes in rigid $[Ln_2O_2]^{2+}$ layers by either internal distortions (around lock in regions) or continual structural change. There is clearly a fine balance between strain energy terms and the energetic penalties of introducing edge-shared tetrahedra.

CONCLUSION

In summary, the origins of transition metal ordering in $Ln_2O_2MSe_2$ type oxychalcogenides has been revealed by investigating a range of solid solutions. Transition metal ordering is determined by the relative sizes of $[Ln_2O_2]^{2+}$ and $[MSe_2]^{2-}$ layers, and can be exquisitely tuned by substitution in either layer. The two extremes of transition metal ordering contain $MSe_{4/2}$ tetrahedra that are exclusively edge-sharing (stripe-like) or exclusively corner-sharing (checkerboard-like). The proportion of the inherently smaller corner-shared motif increases as the transition metal size increases relative to the lanthanide oxide layers. Detailed structural information has been determined for the commensurate compounds $Ce_2O_2Fe_{3/4}Zn_{1/4}Se_2$ (3C-1E), $Ce_2O_2Fe_{1/8}Zn_{7/8}Se_2$ (4C-1E), $Ce_2O_2Zn_{1/6}Mn_{5/6}Se_2$ (5C-1E), $La_2O_2Zn_{1/10}Mn_{9/10}Se_2$ (4C-1E) and $Ce_2O_2CdSe_2$ (1C-0E).

ASSOCIATED CONTENT

Supporting Information

Synthetic conditions for all samples; cell volume and cell parameters of all layered phases; color of samples; an example of the modulation approach to fitting weak satellite peaks; structural parameters and Rietveld refinement profiles for $Ce_2O_2Fe_{3/4}Zn_{1/4}Se_2$ (3C-1E), $Ce_2O_2Fe_{1/8}Zn_{7/8}Se_2$ (4C-1E), $Ce_2O_2Zn_{1/6}Mn_{5/6}Se_2$ (5C-1E), $La_2O_2Zn_{1/10}Mn_{9/10}Se_2$ (4C-1E) and $Ce_2O_2CdSe_2$ (1C-0E); average bond angles around $Ln–O_{4/2}$ tetrahedra in a range of ZrCuSiAs-related compounds. This material is available free of charge via the Internet at http://pubs.acs.org.

AUTHOR INFORMATION

Corresponding Author

*E-mail: john.evans@durham.ac.uk

Present Addresses

Hannah E. Johnston - University of Edinburgh, Joseph Black Building, David Brewster Road, Edinburgh, Scotland EH9 3FJ

Emma E. McCabe - School of Physical Sciences, Ingram Building, University of Kent, Canterbury, UK, CT2 7NH

Notes

The authors declare no competing financial interests.

ACKNOWLEDGMENT

We thank ISIS for neutron time, and EPSRC for funding (EP/J011533/1). Some of these data were collected on the Powder Diffraction beamline at the Australian synchrotron. We thank Ivana Evans, Matthew Tate, Nicola Scarlett and Garry McIntyre for assistance with data collections.

REFERENCES

(1) Hiramatsu, H.; Yanagi, H.; Kamiya, T.; Ueda, K.; Hirano, M.; Hosono, H. *Chem. Mater.* **2008**, *20*, 326-334.

(2) Ueda, K.; Takafuji, K.; Hiramatsu, H.; Ohta, H.; Kamiya, T.; Hirano, M.; Hosono, H. *Chem. Mater.* **2003**, *15*, 3692-3695.

(3) Kamihara, Y.; Watanabe, T.; Hirano, M.; Hosono, H. *J. Am. Chem. Soc.* **2008**, *130*, 3296-3297.

(4) Ijjaali, I.; Mitchell, K.; Haynes, C. L.; McFarland, A. D.; Van Duyne, R. P.; Ibers, J. A. *J. Solid State Chem.* **2003**, *176*, 170-174.

(5) Wang, C. H.; Ainsworth, C. M.; Gui, D. Y.; McCabe, E. E.; Tucker, M. G.; Evans, I. R.; Evans, J. S. O. *Chem. Mater.* **2015**, DOI 10.1021/acs.chemmater.1025b00666.

(6) Peschke, S.; Nitsche, F.; Johrendt, D. *Z. Anorg. Allg. Chem.* **2015**, DOI 10.1002/zaac.201400603.

(7) McCabe, E. E.; Free, D. G.; Evans, J. S. O. *Chem. Commun.* **2011**, *47*, 1261-1263.

(8) Hiramatsu, H.; Ueda, K.; Kamiya, T.; Ohta, H.; Hirano, M.; Hosono, H. *J. Mater. Chem.* **2004**, *14*, 2946-2950.

(9) Tuxworth, A. J.; McCabe, E. E.; Free, D. G.; Clark, S. J.; Evans, J. S. O. *Inorg. Chem.* **2013**, 52, 2078-2085.

(10) Ainsworth, C. M.; Wang, C.-H.; Tucker, M. G.; Evans, J. S. O. *Inorg. Chem.* **2015**, 54, 1563-1571.

(11) Anderson, J. S. Journal of the Chemical Society, Dalton Transactions **1973**, 1107-1115.

(12) Wallwork, K. S.; Kennedy, B. J.; Wang, D. In *Synchrotron Radiation Instrumentation, Pts 1 and 2*; Choi, J. Y., Rah, S., Eds. 2007; Vol. 879, p 879-882.

(13) Schmitt, B.; Bronnimann, C.; Eikenberry, E. F.; Gozzo, F.; Hormann, C.; Horisberger, R.; Patterson, B. *Nuclear Instruments & Methods in Physics Research Section a-Accelerators Spectrometers Detectors and Associated Equipment* **2003**, *501*, 267-272.

(14) Rietveld, H. M. *J. Appl. Crystallogr.* **1969**, *2*, 65.

(15) Coelho, A. A. *J. Appl. Crystallogr.* **2003**, *36*, 86-95.

(16) Coelho, A. A. TOPAS Academic: General Profile and Structure Analysis Software for Powder Diffraction Data, 5th ed.; Bruker AXS: Karlsruhe, Germany, 2012.

(17) Coelho, A. A.; Evans, J. S. O.; Evans, I. R.; Kern, A.; Parsons, S. *Powder Diffr.* **2011**, *26*, S22-S25.

(18) Dollase, W. *J. Appl. Crystallogr.* **1986**, *19*, 267-272.

(19) Pitschke, W.; Hermann, H.; Mattern, N. *Powder Diffr.* **1993**, *8*, 74-83.

(20) Stephens, P. *J. Appl. Crystallogr.* **1999**, *32*, 281-289.

(21) McCabe, E. E.; Free, D. G.; Mendis, B. G.; Higgins, J. S.; Evans, J. S. O. *Chem. Mater.* **2010**, *22*, 6171-6182.

(22) Nitsche, F.; Niklaus, R.; Johrendt, D. *Z. Anorg. Allg. Chem.* **2014**, *640*, 2897-2902.

(23) Shannon, R. *Acta Crystallogr. A* **1976**, *32*, 751-767.

(24) Zhao, J.; Huang, Q.; de la Cruz, C.; Li, S. L.; Lynn, J. W.; Chen, Y.; Green, M. A.; Chen, G. F.; Li, G.; Li, Z.; Luo, J. L.; Wang, N. L.; Dai, P. C. *Nature Mater.* **2008**, *7*, 953-959.

(25) Hsu, F. C.; Luo, J. Y.; Yeh, K. W.; Chen, T. K.; Huang, T. W.; Wu, P. M.; Lee, Y. C.; Huang, Y. L.; Chu, Y. Y.; Yan, D. C.; Wu, M. K. *Proc Natl Acad Sci U S A* **2008**, *105*, 14262-14264.

For Table of Contents Only

The origin of transition metal ordering in $Ln_2O_2MSe_2$ oxychalcogenides has been revealed by investigating a range of solid solutions. Transition metal ordering is determined by the relative sizes of $[Ln_2O_2]^{2+}$ and $[MSe_2]^{2-}$ layers and can be exquisitely tuned by substitution in either layer, leading to an “infinitely adaptive” structural family. The proportion of the inherently smaller corner-shared motif increases as the transition metal size increases relative to the lanthanide oxide layers.